RSC Advances

PAPER

View Article Online
View Journal | View Issue

Check for updates

Cite this: *RSC Adv.*, 2026, **16**, 30435

Investigation of the electronic, magnetic, and thermoelectric characteristics of the transition metal-based double perovskites Ba_2XNbO_6 (X = V, Cr, Mn, and Fe) for spintronic applications

Sajid Rafique,[a] Q. Mahmood,*[bc] Ghulam M. Mustafa, *[a] Hanof Dawas Alkhaldi,[d] A. A. Abd El-Moula,[e] Awatif Alshamari,*[f] Imed Boukhris[g] and Mohd Taukeer Khan[h]

Spin-polarized materials with high Curie temperatures are emerging aspirants for spintronics. In the present work, we conduct first-principles calculations using the WIEN2k code to examine the structural, electronic, magnetic, and thermoelectric properties of Ba_2XNbO_6 (X = V, Cr, Mn, and Fe). The thermodynamic stability is confirmed by the negative enthalpies of formation and the structural stability by the tolerance factor. The range of Curie temperatures (T_c) from 289 K to 325 K for the studied materials allows for room-temperature ferromagnetism. Inferring from their spin-polarized band structures, Ba_2VNbO_6 and Ba_2MnNbO_6 have half-metallic ferromagnetism, and Ba_2CrNbO_6 and Ba_2FeNbO_6 have ferromagnetic semiconductor behavior. The calculated exchange and crystal field energies and exchange constants reveal dominant spin–orbit coupling rather than magnetic ion clustering. The total magnetic moment analysis demonstrates that the magnetic moment ranges from $2.0\mu_B$ to $5.00\mu_B$ for the Fe-based compounds, reflecting the gradual addition of electrons to the 3d orbitals, and its distribution to non-magnetic sites confirms the exchange of electrons. Additionally, these compounds show great potential in thermoelectrics. Ba_2VNbO_6 reached a power factor of 8.60 W mK^{-2} because of its good electrical conductivity and moderate Seebeck coefficient. These results underscore that substituting the B-site elements in Ba_2XNbO_6 (X = V, Cr, Mn, and Fe) can improve the spintronic and thermoelectric properties by modifying the electronic structure, magnetic behavior, and measurable thermoelectric power.

Received 11th March 2026
Accepted 12th May 2026

DOI: 10.1039/d6ra02067d

rsc.li/rsc-advances

1. Introduction

Spintronics is an emerging field of science that has an extensive impact on the emerging features of the electronics industry. Traditional electronic mechanisms are based on the charge of the electron. However, incorporating the spin of the electron in electronic devices gives birth to the new, quickly growing field of spintronics.[1] The benefits of spintronics over traditional electronics are their high speed, small size, low power consumption, and greater efficiency with high robustness.[2] Spintronic devices need spin-polarization (SP) of 100% near the Fermi level (E_F). Hence, we required magnetic materials that offer extraordinary spin-polarization around E_F.[3] For this purpose, the half-metallic ferromagnetic (HMFM) materials are potential candidates showing 100% spin polarization near E_F for one spin configuration and a band gap for the other spin channel. These HMFM materials are more effective when their Curie temperature is greater than room temperature. In such compounds, asymmetry in the spin-polarized density of state (DOS) is witnessed near E_F.[4] Spintronics has unlocked possibilities for manufacturing spin-based electronic devices, including magnetic tunnel junctions (MTJs), spin valves (SVs), and spin transistors (STs), due to the exploration of HMFM materials.[5] Spin-based electronic devices are regulated by controlling spin-polarized currents. Spin-reliant events, including tunnel magnetoresistance (TMR) and colossal magnetoresistance (CMR), depend directly on the design and fabrication of HM materials. In spintronics, the concepts of TMR and CMR are

---

[a] Department of Physics, Division of Science and Technology, University of Education, Lahore, Punjab 54770, Pakistan. E-mail: gmmustafa1025@gmail.com

[b] Basic and Applied Scientific Research Center, Imam Abdulrahman Bin Faisal University, P. O. Box 1982, Dammam, 31441, Saudi Arabia. E-mail: qmmustafa@iau.edu.sa

[c] Department of Physics, College of Science, Imam Abdulrahman Bin Faisal University, P. O. Box 1982, Dammam, 31441, Saudi Arabia

[d] Department of Science and Technology, University College at Nairiyah, University of Hafr Al Batin (UHB), Nairiyah 31981, Saudi Arabia

[e] Physics Department, College of Science, Jouf University, 2014, Sakaka, Jouf, Saudi Arabia

[f] Department of Physics, College of Science, Northern Border University, P.O. Box 1321, Arar, 91431, Kingdom of Saudi Arabia. E-mail: Awatef.Alshammri@nbu.edu.sa

[g] Department of Physics, Faculty of Science, King Khalid University, P.O. Box 960, Abha, Saudi Arabia

[h] Department of Physics, Faculty of Science, Islamic University of Madinah, Al Jamiah, Madinah, 42351, Saudi Arabia

fundamental in high-density magnetic data storage devices.[6] In numerous types of materials, such as spinel chalcogenides, double perovskites (DPs), and transition metal oxides, scientists have used the idea of half-metallicity theoretically and experimentally. Zn-based spinel chalcogenides were predicted to be potential applicants because they respond at high temperatures. Ferromagnetic materials with frustrated ferromagnetism play a crucial role in manipulating spintronic gadgets.[7,8] Half metallic ferromagnetic materials include $SnCo_2O_4$, Sr_2FeMoO_6, and $BaTiO_3$ and have the potential to solve this puzzle.[9] In recent years, a lot of studies have been carried out on spinel compounds owing to their superior thermoelectric (TE) and FM characteristics.[10] HMFM has also been investigated in the context of the hybridization of atomic states. The HMFM response of these materials was inspected by examining the crystal field energy (CFE) and the Jahn–Teller effect (JTE).[11] HMFM was observed in double perovskites, which have potential for spintronics due to their stable structure, high Curie temperature (T_c), and cost-effectiveness.

Perovskite materials are categorized by the 3-D connection of their metallic cations enclosed by an octahedron of halogen anions due to their unique crystal structure.[12] The predominantly investigated single perovskites are mostly represented by the general formula ABX_3, where the A and B sides are cations and X is an anion.[13,14] A new configuration ($A_2BB'X_6$) has been established by doubling the atoms, where B and B′ are dissimilar cations.[15] Furthermore, FM character at T_c (635 K, 725 K) is displayed by the DP with Sr_2CrYO_6 (Y = Re and Os) composition.[16] To explain their TE and magnetic behaviors, an assortment of DPs has been investigated.[17,18]

Several first-principles investigations have explored the magnetic and thermoelectric properties of double perovskite oxides using density functional theory (DFT)-based approaches. Fang *et al.* investigated Sr_2FeMO_6 (M = Mo, W, and Re), studied the role of 5d electrons in controlling their magnetoresistance characteristics, and noticed their Tc values in the range of 410 K to 419 K.[19] In the stable ferromagnetic phase, the magnetic moments were computed to be $0.39/0.22/-0.86\mu_B$ for Mo/W/Re, respectively. The change of magnetic moments (MMs) to non-magnetic (NM) nodes confirmed the spin of electrons, which allowed their customizable use in quantum gadgets.[20] For instance, through the use of the FP-LAPW approach, Sahnoun *et al.* found that Ba_2FeMoO_6 has a half-metallic ferromagnetic state where the magnetic moment on Fe sites is measured at $3.631\mu_B$ but the Mo sites do not exhibit measurable magnetism. Moreover, it behaved like an n-type semiconductor up to 1200 K, and, at 200 K, its high *ZT* value was close to one.[21] Similarly, applying DFT with exchange–correlation functionals, Khandy and Gupta studied Sr_2HoNbO_6 and found it to be a ferromagnetic semiconductor with a wide band gap of 3.6 eV and a total magnetic moment of $4.0\mu_B$, mostly contributed by Ho ($\mu_{Ho} = 3.95\mu_B$). The analysis of their thermoelectric properties indicated that these have p-type conductivity, with a peak *ZT* value of about 0.97 at room temperature.[22] Similarly, Blaha *et al.* used FP-LAPW within the GGA and mBJ methods to study Sr_2TiCoO_6, showing it had magnetic behavior with $1\mu_B$, was both strong and brittle, and its power factor increased until 1000 K.[23] Agouri *et al.* carried out a study on Sr_2CeVO_6 and Ba_2CeVO_6 that identified them as stable cubic magnets and found they have half-metallic characteristics, are ductile, and have high power factors due to their n-type conductivity mostly through the different oxidation states of vanadium.[24] Mahmood employed the WIEN2k and BoltzTraP codes based on DFT to explore the physical characteristics of Ba_2XMoO_6 (X = Cr, Mn, Fe, and Co) which exhibited their half metallic ferromagnetism with a spin-polarization of 100%, high Curie temperatures (340–313 K), magnetic moments ranging from 3.0 to $5.0\mu_B$, and negative formation energies, indicating their thermodynamic stability and excellent prospective for thermoelectric and spintronic devices.[25] In a similar context, Caid *et al.* used the FP-LAPW approach in the GGA and GGA + *U* frameworks to examine the electronic and magnetic behavior of Ba_2ZrFeO_6. Their calculations revealed a transition from metallic to half-metallic ferrimagnetism upon including the Hubbard *U* term, yielding a direct band gap of 1.98 eV (up spin) and total magnetic moment of $-4.0\mu_B$, thereby reinforcing the material's suitability for magneto-electronic applications.[26] Furthermore, Ishfaq *et al.* applied DFT with the PBE-GGA functional using WIEN2k and BoltzTraP to investigate A_2HfNiO_6 (A = Ba, Ca, and Sr), which demonstrated their half-metallic semiconducting nature with substantial band gaps of 3.70, 2.91, and 2.42 eV, respectively, along with total magnetic moments of approximately $4.0\mu_B$, suggesting robust magnetic ordering conducive to spintronics and thermoelectrics.[27] Additionally, Khandy and Gupta carried out a comprehensive study on Ba_2XNbO_6 (X = Ho and Yb) using the TB-mBJ potential and GGA and GGA + *U*, alongside density functional perturbation theory (DFPT) for phonon dispersion analysis. Their findings confirmed the material's half-metallicity, with spin moments of 4 and $1\mu_B$, dynamic stability, and high Seebeck coefficients ($-347.65\ \mu V\ K^{-1}$ for Ho and $-261.11\ \mu V\ K^{-1}$ for Yb), thus emphasizing their dual applicability in the spintronic and thermoelectric domains.[28] Cherif *et al.* investigated the Ba_2FeWO_6 double perovskite and reported that it exhibits an indirect band gap of 0.91 eV along the L–X direction, along with a net magnetic moment of $4\mu_B$. These findings, combined with its low brittleness and favorable elastic properties, suggest its potential suitability for low-temperature thermoelectric applications.[29] Similarly, Ullah *et al.* carried out a DFT study on Ba_2EuMoO_6, revealing it as a thermodynamically stable ferromagnet in the cubic phase characterized by a half-metallic nature, total magnetic moment of about $7\mu_B$, and a direct down-spin band gap of 2.17 eV. Importantly, its high n-type thermoelectric performance was reflected in a *ZT* value of 0.91, indicating promising applications in thermoelectric energy conversion.[30] In another study, Ali *et al.* explored Ba_2GdXO_6 (X = Nb and U) using both the GGA + *U* and HSE06 functionals and found Ba_2GdNbO_6 to be a direct band gap semiconductor (E_g ranging from 2.3 to 5.38 eV), while Ba_2GdUO_6 displayed half-metallic behavior. Both compounds exhibited ferromagnetic ground states with total magnetic moments of $7\mu_B$ and $8\mu_B$, respectively. Notably, Ba_2GdUO_6 demonstrated superior thermoelectric performance due to its higher power factor and *ZT*.[31] Furthermore, Nadeem *et al.* investigated the series Sr_2NbXO_6 (X = Mn, Fe, Co, and Ni) and reported that all compositions are half-metallic ferromagnets, with total magnetic moments of 6, 5, 4, and $2\mu_B$, respectively. These materials also displayed significant thermoelectric performances, indicating their potential use in both spintronic and energy conversion applications.[32] A theoretical investigation of 4d-series transition metal doped graphene has been executed, in which the hybridization, magnetic moments, and Curie temperatures are explained thoroughly. The Nb-, Mo-, and T_c-doped graphene have Curie temperatures of 83, 354, and 36 K, respectively, with a doping concentration of 3.125%.[33] Similarly, Mn doping with a concentration of 5.56% has a Curie temperature of 735 K, which increases rapidly when increasing the doping to 12.5% to a value of 1120 K.[34]

To the best of our knowledge, no theoretical investigation has been dedicated to exploring the various physical aspects of $Ba_2XNb_2O_6$ (X = V, Cr, Mn, and Fe) double perovskites. Therefore, the current study aims to theoretically investigate the structural, electronic, magnetic, and transport properties of $Ba_2XNb_2O_6$ (X = V, Cr, Mn, and Fe) DPs to examine their potential for spintronics and spintronic devices.

2. Computational methods

In the current research work, the various physical characteristics of the electronic and magnetic responses of DPs $Ba_2XNb_2O_6$ (X = V, Cr, Mn, and Fe) were explored using spin-polarized DFT.[35,36] The full-potential linearized augmented plane wave plus local orbital (FP-LAPW + lo) technique was used to compute the structural and energetic characteristics using the WIEN2k software.[37] By applying the PBEsol approximation, the structural optimization to pin the ground state energy was performed.[38] Since the TB-mBJ potential is an effective functional to more precisely compute the electronic band structure (BS), it has been utilized to calculate the electronic band structure.[39,40] In the present study, the Perdew–Burke–Ernzerhof (PBE) exchange–correlation function was used for structural optimization, yielding reliable estimates of lattice parameters, bulk moduli, and ground state energies. For electronic structure analysis and the evaluation of key physical properties, the modified Becke–Johnson potential (mBJ) was utilized. The mBJ approach offers a favorable balance between computational efficiency and accuracy, particularly when compared to more resource-intensive methods such as generalized gradient approximation (GGA) with onsite Coulomb correction (GGA + *U*) and hybrid functionals like HSE06. Notably, mBJ delivers band gap predictions and electronic state distributions that exhibit excellent agreement with experimental data, especially for semiconductor systems and transition-metal-based compounds. While GGA + *U* is more appropriate for systems containing localized f-electrons, such as rare earth or 5d transition elements, and HSE06 provides improved accuracy for a wide range of materials, these methods often require significantly higher computational resources and present greater complexity in practical implementation. A comparative assessment reveals that mBJ not only accelerates the convergence of electronic calculations but also simplifies the computational workflow, thereby offering a pragmatic and robust alternative for accurate electronic structure predictions, especially in studies prioritizing efficiency without compromising predictive reliability. The TB-mBJ is a versatile potential that gives accurate band gaps for transition metal-based calculations such as the GGA + *U* and HSE06 potentials. Zaari *et al.* compared the results of the magnetic moment and band gap of $CdFe_2O_4$ by calculating them with the TB-mBJ and GGA + *U* potentials. Band gaps of 1.88 eV and 1.56 eV are reported for TB-mBJ and GGA + *U*, respectively. The total magnetic moments of $4.17\mu_B$ and $4.18\mu_B$ were calculated by GGA + *U* and TB-mBJ and are very close to each other. The advantage of GGA + *U* for heavy elements is that it includes d and f states more accurately in the calculation system. The final analysis of Zaari *et al.* was that, after including some advantages and deficiencies of these two potentials, they are similar in accuracy.[41] Furthermore, Li *et al.* compared the accuracy and calculation errors of the band gaps for many and varied materials, such as transition metal-based systems and mixed and doped materials. They report that the band gaps had 25% error for both the HSE06 and TB-mBJ potentials. The positive point of the TB-mBJ potential is its lower computational cost.[42]

During optimization, as an input parameter, the values for maximum wave vector ($K_{\max}$) and muffin-tin radius (R_{MT}) were set as $R_{\mathrm{MT}} \times K_{\max} = 8$. The values of R_{MT} for V, Cr, Mn, and Fe were fixed as 1.85, 2.1, 2.5, and 2.37 a.u, respectively. The cut-off energy criteria, Gaussian factor, and angular momentum vector were set as −6.0 Ry, 18, and 10, respectively. Since the size of the *k*-mesh is crucial for computation, for the present calculation, 1000 *k*-points were selected for the finest energy convergence. Finally, for the calculation of transport parameters, the Maxwell–Boltzmann theory-based BoltzTrap code was used with a relaxation time constant of 10^{-14} s.[43] In our calculations, a constant relaxation time of $\tau = 10^{-14}$ s has been used based on the Boltzmann transport framework. We acknowledge that this approximation neglects the dependence of τ on carrier type, temperature, and scattering mechanisms, which reduces the accuracy of calculations. This limitation is mentioned in the revised manuscript. In reality, electrons and holes have different relaxation times, which are calculated by deformation potential theory. This is computationally very expensive and beyond the scope of the present study and our expertise. Therefore, we will clearly mention in the revised manuscript that the calculated transport coefficients give semi-quantitative trends rather than absolute values. The carrier's concentration ($\sim 10^{19}$ cm^{-3}) is not fixed as an intrinsic property; it varies with chemical potential (μ). However, for smooth calculations by the BoltzTraP code, the carrier's concentration ($\sim 10^{19}$ cm^{-3}) was adjusted at zero chemical potential, where it remains almost constant during the calculations. This is also the limitation of classical Boltzmann theory-based analysis. Finally, it is concluded that the Boltzmann theory-based BoltzTraP code only provides accurate trends of thermoelectric coefficients instead of their absolute values.

We kept the supercell size at 2 × 2 × 2, number of atoms at 80, and the timesteps at 1 fs with a total simulation time of 20 ps and used the Langevin (*NPT*) thermostat for the AIMD calculations. For the input of the ShengBTE code, the third-order interatomic force constants were calculated by Esfarjani *et al.* using their methodology.[44] In the calculations of the third-order IFCs, we replaced two atoms up to the 5th nearest neighbors. There was a minute deviation in lattice thermal conductivities at 300 K. For the 5th nearest neighbor displacement consideration, we obtained well-converged lattice thermal conductivities with a K-mesh order of 12 × 12 × 12.

3. Results and discussion

3.1. Structural properties

Fig. 1 illustrates the ball-and-stick (left) and polyhedral (right) models of the unit cell of the investigated Ba_2XNbO_6 (X = V, Cr, Mn, and Fe) in the cubic phase. In this unit cell, red, gold, green, and purple-colored balls designate the Ba, X, Nb, and O atoms, respectively. These DPs belong to the $Fm\bar{3}m$ (225) space group. The basic cubic structure of these DPs is a framework in which octahedra share their corners with a monovalent Ba atom placed at the center of the octahedral void. Twelve O atoms are positioned in the surroundings of each Ba atom, while six O atoms are placed in the surroundings of each X and Nb atom. It can be observed from Fig. 1 that atoms of X and Nb are placed at each octahedron's center. The positions of Wyckoff sites (0.25, 0.25, 0.25), (0, 0, 0), (0.5, 0.5, 0.5), and (x, 0, 0)[45] are engaged by the Ba, X, Nb, and O atoms, respectively.

The volume optimization procedure was performed under PBE-GGA[46] to acquire the structural parameters, including the lattice constant (a), bulk modulus (B), ground state energy (E_g), enthalpy of formation (ΔH_f), and Curie temperature (T_c). The data of volume *versus* energy was fixed with Birch–Murnaghan's equation of state[47] to find the ground state energy value, volume, and bulk modulus. The Curie temperature was calculated by the mean field approximation of the Heisenberg model, which has an empirical formula $T_c = 2\Delta E/3xK_B$. where ΔE is the difference in the ground state energies of the FM and AFM states. The 'x' represents the concentration of magnetic ions in the formula unit, and K_B represents the Boltzmann constant. The calculated values of the Curie temperature are mentioned in Table 1. Fig. 2(a–d) shows volume optimization graphs in the ferromagnetic (FM) and anti-ferromagnetic (AFM) phases which exhibit that all these compositions are more stable. Energy differences of 0.102 eV, 0.201 eV, 0.1156 eV, and 0.129 eV were calculated for the V-, Cr-, Mn-, and Fe-doped double perovskite oxides. This is because more energy is released during the formation of the FM phase than the AFM phase, highlighting that FM states are more stable and have potential for practical uses. Furthermore, it is noted that the Fe-based composition is more stable in its FM phase because more energy is released when X is replaced by Fe instead of V, Cr, and Mn.

Table 1 Parameters a, B, T_c, and ΔH_f for Ba_2XNbO_6 (X = V, Cr, Mn, and Fe)

Compound	a (Å)	Literature a (Å)	B (GPa)	ΔH_f (eV)	T_c (K)
Ba_2VNbO_6	8.26	8.11 (ref. 46)	151	−3.11	325
Ba_2CrNbO_6	8.24	—	162	−3.01	305
Ba_2MnNbO_6	8.16	8.12 (ref. 47)	165	−2.93	302
Ba_2FeNbO_6	8.14	8.11 (ref. 47)	169	−2.89	289

Table 1 lists the computed values of the lattice constant (a), bulk moduli (B), and formation energy (ΔH_f) from the optimized structures in the FM state. The Curie temperature is the key parameter that leads to ensuring the practical implementation of any material that has been computed using the Heisenberg formalism.[48] The computed values of the lattice constant are noted as 8.26 Å, 8.24 Å, 8.16 Å, and 8.14 Å with corresponding T_c values of 325 K, 305 K, 302 K, and 289 K for Ba_2VNbO_6, Ba_2CrNbO_6, Ba_2MnNbO_6, and Ba_2FeNbO_6, respectively. The value of B increases as the value of the lattice constant decreases because the expansion of the unit cell makes it less hard.[49] The computed values of B are 151 GPa for Ba_2VNbO_6, 162 GPa for Ba_2CrNbO_6, 165 GPa for Ba_2MnNbO_6, and 169 GPa for Ba_2FeNbO_6. The thermodynamic viability of newly engineered perovskite compounds can be rigorously assessed through the evaluation of their formation enthalpy (ΔH_f). A negative value of ΔH_f is indicative of intrinsic thermodynamic stability, signifying that the material is energetically favorable to form under standard conditions.[50] For the investigated double perovskites, the calculated formation energies were found to be −3.11 eV for Ba_2VNbO_6, −3.01 eV for Ba_2CrNbO_6, −2.93 for Ba_2MnNbO_6, and −2.89 eV for Ba_2FeNbO_6. These results confirm the

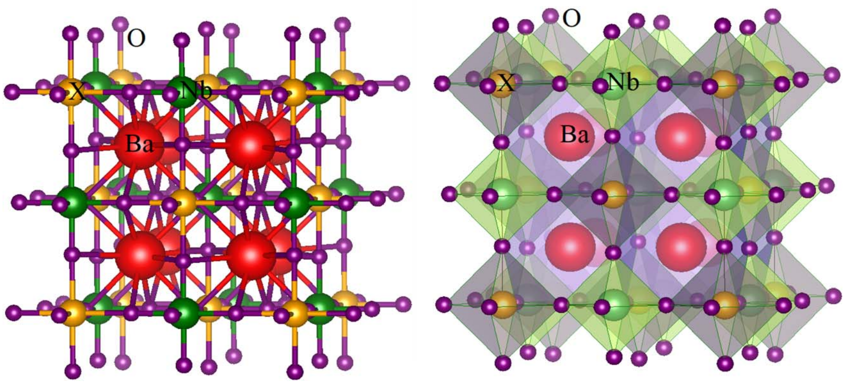

Fig. 1 Ball-and-stick and polyhedral models of the double perovskites Ba_2XNbO_6 (X = V, Cr, Mn, and Fe).

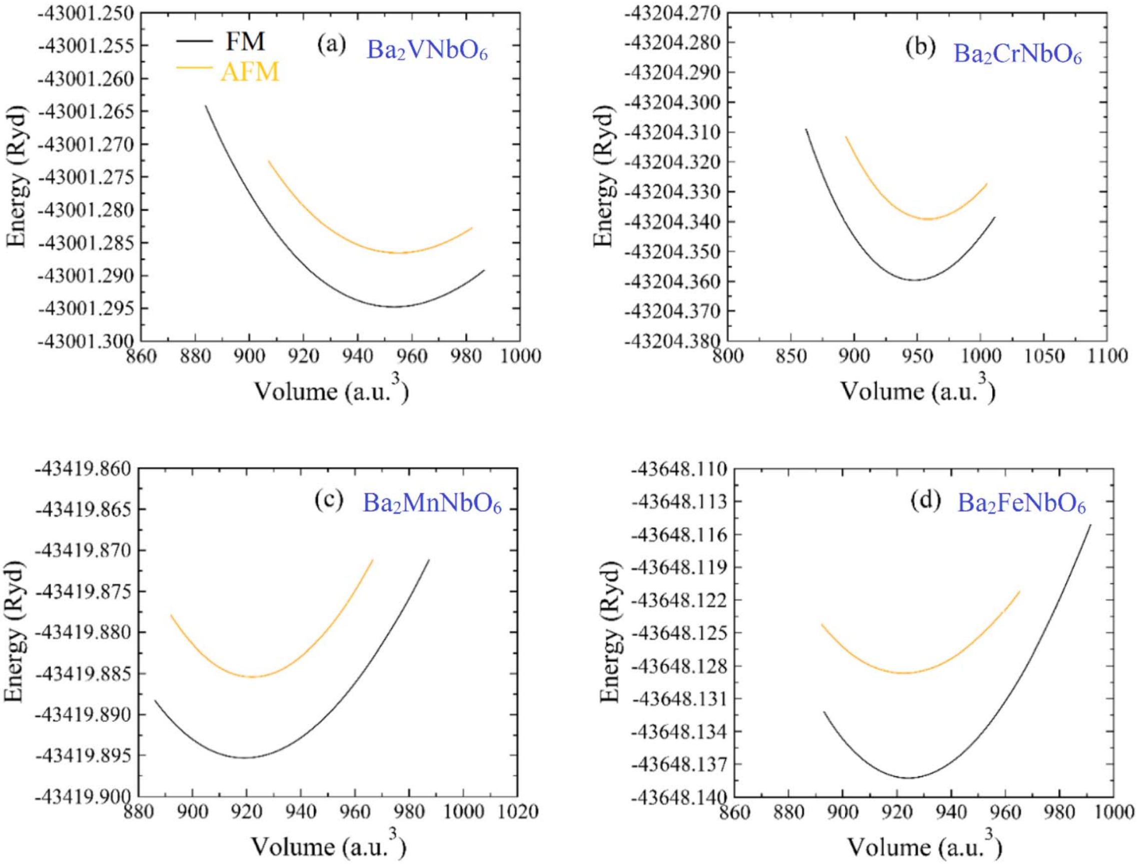

Fig. 2 Relationships between the volume and total energy of Ba_2XNbO_6, where X = (a) V, (b) Cr, (c) Mn, and (d) Fe.

thermodynamic stability of all four compositions, with a slight decrement in stability observed across the series from vanadium to iron. The formation enthalpy was computed using the following expression:

$$\Delta H_f = E_{total}(Ba_aX_bNb_cO_d) - aE_{Ba} \pm bE_X \pm cE_{Nb} \pm dE_O, \quad (1)$$

where E_{total} denotes the total energy of the compound, and E_{Ba}, E_X, E_{Nb}, and E_O represent the reference energies of individual elements Ba, X, Nb, and O in their standard states, respectively. The computed ΔH_f values, summarized in Table 1, consistently exhibit negative magnitudes, reinforcing the thermodynamic favorability of the synthesized perovskites. Moreover, the observed trend in formation energy suggests a progressive decrease in thermodynamic stability as the B-site transition metal shifts from V to Fe. Furthermore, the magnetic properties of double perovskite oxides are fundamentally significant for the development of next-generation spintronic devices. A pivotal parameter in evaluating their functional applicability is the Curie temperature (T_c), which delineates the thermal boundary between the ferromagnetic and paramagnetic phases.[51] For spintronic components to operate reliably at or above ambient conditions, maintaining robust spin polarization necessitates materials with a T_c exceeding room temperature. In this context, the double perovskite compounds Ba_2VNbO_6, Ba_2CrNbO_6, Ba_2MnNbO_6, and Ba_2FeNbO_6 exhibit promising characteristics, with experimentally determined Curie temperatures of approximately 325, 305, 302, and 289 K, respectively. These values, ascertained through theoretical modeling based on the Heisenberg exchange interaction framework, underscore the thermal resilience of these systems. The relatively high T_c values facilitate efficient spin injection and retention under operational conditions, thereby supporting their integration into key spintronic architectures such as magnetic tunnel junctions and spin-effect transistors. The thermal stabilities of their ferromagnetic order position these materials as viable candidates for practical spin-based electronics.[52]

Along with thermodynamic stability, the thermal stability of the lattice is also extremely important. Here, therefore, AIMD calculations were performed to ensure thermal stability. For this purpose, the total energy (eV) was calculated again in every simulation (fs), as shown in Fig. 3(a–c). It is obvious from Fig. 3(a–c) that the energy variation is negligible for the simulation time and remains almost constant for the 300, 500, and 700 K temperatures. In addition to the above, there is no bond breaking or other phases produced, which also ensures the thermal stability of the studied materials.

3.2. Electronic properties

Electronic band structure plays a key role in optimizing the electrical and optical behaviors of any material, and Fig. 4(a–d)

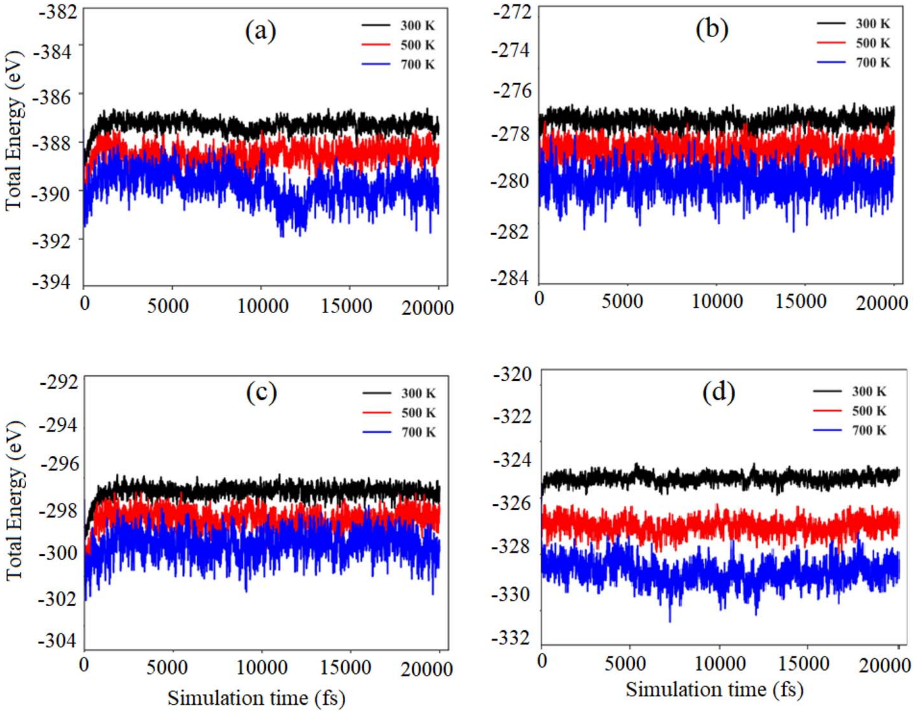

Fig. 3 *Ab initio* molecular dynamics calculations for the simulation time and total energy of Ba_2XNbO_6, where X = (a) V, (b) Cr, (c) Mn, and (d) Fe at 300, 500, and 700 K.

depicts the electronic band structures of the DP materials. Fig. 4(a–d) represents the spin-polarized (SP) band diagrams for the up- and down-spin states of the Ba_2VNbO_6, Ba_2CrNbO_6, Ba_2MnNbO_6, and Ba_2FeNbO_6 compositions, respectively.

The pink and green colors depict the electronic BS in the up- and down-spin states, respectively. The Ba_2VNbO_6 and Ba_2MnNbO_6 compositions exhibited a half-metallic ferromagnetic (HMFM) nature because the spin-up states of both compositions depict a metallic nature with bands crossing the Fermi level (E_F), and the down-spin states of both compositions show a bandgap, revealing a semiconducting nature.[53] It was found that all the compositions have an indirect band gap nature. The Ba_2CrNbO_6 and Ba_2FeNbO_6 compositions show a ferromagnetic semiconducting (FMSC) nature.[54] The spins of their electrons

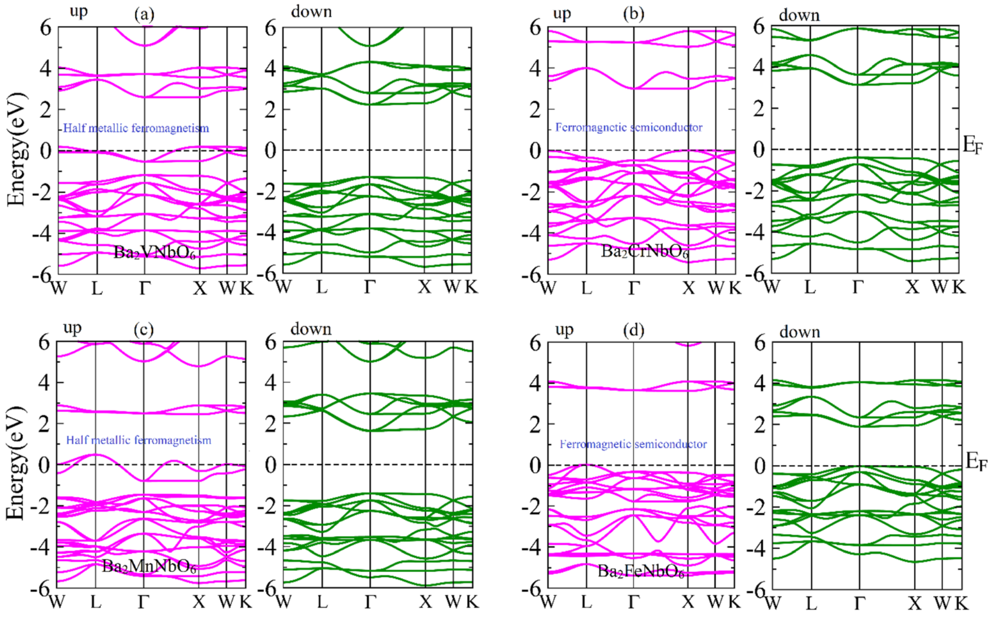

Fig. 4 Spin-polarized electronic band structures of the double perovskite materials Ba_2XNbO_6, where X = (a) V, (b) Cr, (c) Mn, and (d) Fe.

are aligned in the same direction throughout the material; therefore, these materials preserve ferromagnetic ordering. For a detailed view of the individual contributions of the states to ferromagnetism, the density of states of the studied materials are plotted in Fig. 5(a–d).

Fig. 5(a) depicts the total (TDOS) and partial (PDOS) density of states of Ba_2VNbO_6. The TDOS plot illustrates the total dispersion of electronic states from all atoms and orbitals in the Ba_2VNbO_6 composition. The energy levels spread from −6 eV to +6 eV and enclose mutually occupied and unoccupied states compared to E_F. The vertical dotted line in the graph represents the E_F. The completely occupied states are situated below the E_F, while the unoccupied states are located above the E_F. The peaks in the graph designate areas with greater electronic state accessibility, and low DOS areas are shown by valleys. The PDOS plot for V indicates that the density of the 3d-t_{2g} states is a maximum at E_F. These states are responsible for the metallic nature of Ba_2VNbO_6 in the up-spin configuration, whereas in the down-spin channel, these states lie deep in the conduction band, forming the band edges for this composition, and thus are crucial for controlling the conductivity of this composition. The density of the 3d-e_g states is small compared to 3d-t_{2g} and lies in the conduction band in the range of 2.5 to 3.5 eV. Looking at the PDOS plots of 6s-Ba and 2p-O, it is noted that the DOS of 2p-O is larger and particularly significant in the valence band (VB) in both spin configurations in the range of −1.0 to −5.5 eV, and these states are mostly localized in energy. Furthermore, a small peak close to −4 eV due to the 2p orbitals of the O atom is also observed in the graph, indicating that the O atoms are assisting the bonding state at this energy range. The 2p-O states play an auxiliary role compared to the transition metals in determining the total electronic characteristics which is revealed by the less pronounced peak of O compared to the Ba contribution. To see the contribution of the Nb atoms to the band formation, its PDOS plot is presented in Fig. 5, where it is witnessed that the t_{2g} states of Nb have a high density of states in the conduction band around 4 eV, whereas a small contribution to the valence band edge formation is witnessed. In contrast, a significant contribution is observed in the VB in the energy range of −4.8 to −5.7 eV.

Fig. 5(b) is divided into four parts comprising the TDOS plots of Ba_2CrNbO_6 and the PDOS plots of Cr, Ba, O, and Nb, respectively, in both spin channels. The ferromagnetic semiconducting nature of this composition is again confirmed from this figure. In the up-spin configuration, t_{2g}-Cr states form the VB edge, whereas the CB edge is made by the e_g states of Cr. However, the density of states of t_{2g} in both spin channels is high compared to that of the e_g states. Similarly, in the case of Nb, the t_{2g} states are closer to E_F in the VB as compared to the t_{2g} states. In the case of O, the energy states are spread in the energy range of 0–5.5 eV in both spin channels. The existence of the energy states of O and transition metals like Cr and V in the same energy range affirms the formation of CrO_6 and NbO_6 octahedra in the composition Ba_2CrNbO_6.

Fig. 5(c) represents the computed TDOS plus the PDOS of the individual atoms of Ba_2MnNbO_6. The calculated TDOS indicates a half-metallic ferromagnetic character, confirmed through the calculated DOS of the up- and down-spin configurations. This is because, in up spin, the DOS crosses the E_F, revealing the metallic nature, whereas, in the down-spin

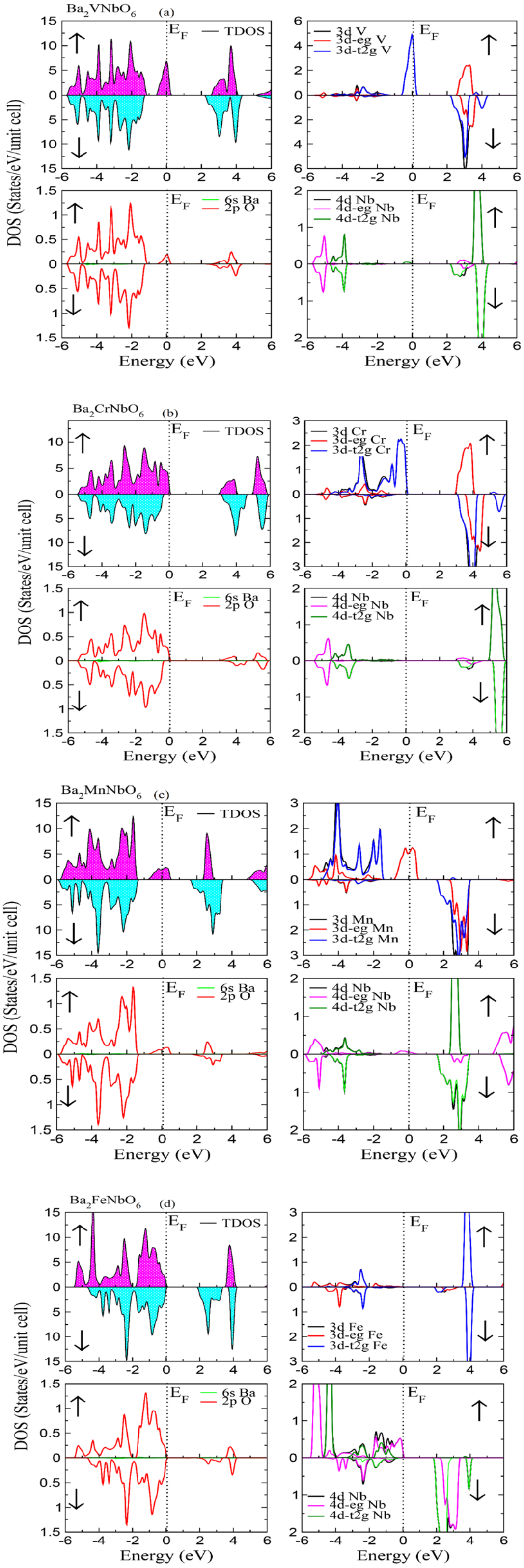

Fig. 5 TDOD and PDOS graphs for (a) Ba_2VNbO_6, (b) Ba_2CrNbO_6, (c) Ba_2MnNbO_6, and (d) Ba_2FeNbO_6.

configuration, the energy states appear away from the E_F, indicating an insulating nature. From the PDOS, we see the individual contributions of atoms to the DOS. The 3d state of Mn is split into 3d-t_{2g} and 3d-e_g states. It is clear from the plot that the 3d-e_g states of Mn cross the Fermi level and are responsible for the metallic behavior of this composition. The 2p-O states also cross the Fermi level in the same manner as the 3d-Mn states, indicating the bonding interaction between Mn and O in the formation of MnO_6 octahedra. It is noted from the graph that when Cr is replaced with Mn, the 6s state of Ba and the 2p state of O show similar behaviors in the valence band. Moreover, the DOS due to the 4d-state and its substates 4d-t_{2g} and 4d-e_g states of the Nb atom were also examined. In the CB, the contribution of the 4d-t_{2g} states of Nb is more significant than that of the e_g-Nb states.

The graph of the TDOS and PDOS for Ba_2FeNbO_6 is depicted in Fig. 5(d). It is observed that when the Cr is replaced with Fe, the DOS is moved toward the E_F in both the valence and conduction bands, confirming that the studied materials have a ferromagnetic semiconducting nature. The Fe has an extra electron compared to the Cr that is responsible for better exchange splitting in the Fe-based composition. Furthermore, the contributions to the DOS for the spin up and down states from the sub-orbitals of the Fe atom are shown, revealing that the 3d-e_g orbital of Fe has a major contribution in the valence band from 0 to −5.5 eV, but it shows a minor contribution in both spin channels in the conduction band. On the other hand, the 3d-t_{2g} orbital shows sharp peaks in the conduction band while showing a slight contribution in the valence band in the energy range of approximately 0 to −3 eV. Furthermore, it is observed that the 6s of Ba has a weaker contribution to the valence band compared to the O atoms, while, in the conduction band, it exhibits a smaller contribution. In addition, the contribution from the 4d-e_g and 4d-t_{2g} orbitals of Nb is examined, and the 4d-e_g orbital extensively participates in the valence band starting from E_F to −5 eV, as well as showing sharp peaks in both spin channels. This might be due to the strong hybridization of the 4d-e_g orbital of Nb with the 2p orbitals of O.[55] In the DPs, the odd and even numbers of electrons of transition metal d-states decide the half-metallic and magnetic semiconducting behaviors because they reveal the filling of the t_{2g} and e_g states due to the exchange splitting process. The odd number of electrons in V (d^3) and Mn (d^5) partially fills one channel to endow insulating characteristics, and the other channel is filled unevenly, which leaves the electrons in bands that cross the Fermi level. Therefore, it produces metallic conduction on one channel (spin up) and insulating behavior on the other channel (spin down). In contrast, Cr (d^4) and Fe (d^6) have an even number of electrons, which fill the t_{2g} and e_g states symmetrically with fully occupied bands. This fact creates band gaps in both spin channels, ensuring magnetic semiconducting behavior. Therefore, an odd number of electrons makes one channel metallic, while an even number of electrons makes it filled, which supports semiconducting behavior.

3.3. Magnetic properties

The magnetic characteristics of any material are quantified in terms of exchange energy and constants, along with their magnetic moments. Under the effects of the high spin orientation, the octahedral assembly of XO_6 (X = V, Cr, Mn, and Fe) ions split the 4d-states of V, Cr, Mn, and Fe to degenerate triplet and doublet states, where the degenerate triplet states are represented by d_{xy}, d_{yz}, and d_{zx} and the doublet degenerate states are designated by $d_{x^2-y^2}$ and d_{z^2}, respectively. The high spin effect further divides this degeneracy into low and high-energy states, where low-energy states represent the triplet states and high-energy states signify the doublet states. A crystal field is generated due to this splitting of states, which is calculated through the t_{2g} and e_g states. The difference between the t_{2g} and e_g states gives the crystal field splitting energy (ΔCF) for the corresponding spin channels. The following formulas are used to calculate the crystal field energy:

$$\Delta_{CF}^{\uparrow} = t_{2g}^{\uparrow} - e_g^{\uparrow} \text{ and } \Delta_{CF}^{\downarrow} = t_{2g}^{\downarrow} - e_g^{\downarrow}, \tag{2}$$

where $\Delta_{CF}^{\uparrow}$ and $\Delta_{CF}^{\downarrow}$ represent the crystal field splitting energies for the up- and down-spin configurations, respectively. The ΔE_{CF} value is inferred from the splitting of the triplet and doublet states in the same spin presentation.[56] Table 2 shows the values of ΔE_{CF} for various compositions, and these values were found to be −2.76, −3.38, −1.51, and 0.00 for Ba_2VNbO_6, Ba_2CrNbO_6, Ba_2MnNbO_6, and Ba_2FeNbO_6, respectively, where the negative sign reveals the stabilizing nature of the ligand field on the collective energy of the d-orbitals. The reason

Table 2 Exchange energies and constants and magnetic moments for Ba_2XNbO_6 (X = V, Cr, Mn, and Fe) in μ_B

Parameter		Ba_2VNbO_6	Ba_2CrNbO_6	Ba_2MnNbO_6	Ba_2FeNbO_6
Exchange energy and constants	$\Delta(C_F)$	−2.76	−3.38	−1.51	0
	$\Delta_x(d)$	−3.05	−4.1	−2.79	0
	$\Delta_x(pd)$	−1.23	−0.29	−1.35	0
	$N_o\alpha$	−0.2	−0.51	−0.22	−0.42
	$N_o\beta$	−0.58	−0.14	−0.29	−0.04
Magnetic moments	MM_{total}	2.0	3.0	4.0	5.0
	MM_{int}	0.316	0.186	0.231	0.006
	MM_{Ba}	0.002	0.005	0.003	0.004
	MM_{Nb}	0.045	0.007	0.072	0.023
	MM_X	1.842	2.706	3.791	4.184
	MM_O	−0.033	−0.016	−0.015	−0.134

behind the negative sign is that ligands give electrons to the central metal ion; due to this, the collective system's energy becomes lower, resulting in the negative value of the ΔE_{CF}.[57] The d-orbital of the Cr-based composition is more stable than those of V, Mn, and Fe, as shown by the corresponding values of ΔE_{CF} due to their strong crystal field splitting. Moreover, it is noted that the value of ΔE_{CF} is zero in the case of the Fe-based composition, which reveals that the effect of the ligand field on the d-orbitals of Fe is zero, resulting in no crystal field splitting. Furthermore, the values of the direct Δ_x(d) and indirect Δ_x(pd) exchange energies, which arise due to the exchange splitting of d-orbitals and exchange splitting due to pd-hybridization, are tabulated in Table 2. The higher value of the Δ_x(d) highlights exceptional magnetic performance due to stronger exchange interaction in d-orbitals, and the highest is found in the Cr-based composition with a value of −4.10 as compared to V, Mn, and Fe, whose values are −3.05, −2.79, and 0.00, respectively. The larger value of the Δ_x(pd) reveals stronger pd-hybridization, which contributes to the magnetic interactions and is observed in the Mn-based composition with a value of −1.35. The CB edge splitting ΔE_C and VB edge splitting ΔE_V help to calculate the exchange constants $N_o\alpha$ and $N_o\beta$ using the following expressions:

$$N_o\alpha = \frac{\Delta E_C}{x\langle S\rangle} \text{ and } N_o\beta = \frac{\Delta E_v}{x\langle S\rangle}, \tag{3}$$

where x denotes the magnetic ion concentration and $\langle S\rangle$ represents the average magnetic moments of the magnetic ions. The strength of magnetization is measured using constant exchange values.[58] Generally, positive $N_o\alpha$ values and negative $N_o\beta$ values show half-metallic ferromagnetism of materials due to the dominance of s–d coupling in the CB and p–d coupling in the VB. However, the quantum confinement effect makes $N_o\alpha$ negative due to the negative value of ΔE_C.[59] The calculated values of $N_o\alpha$ and $N_o\beta$ are given in Table 2. The down-spin configuration promotes a double exchange mechanism to endow ferromagnetic character,[60] which is verified by the negative $N_o\beta$ values. To determine the nature of the magnetism, the total and partial magnetic moments were calculated for each composition and are presented in Table 2. It is observed that inside the V, Cr, Mn, and Fe-based compositions, the total magnetic moments (MM) are found to be 2, 3, 4, and 5μ_B, respectively. These values align well with other reported values.[61,62] Furthermore, it is noted that the highest values of magnetism primarily come from the X atoms. The magnetic moment values that come from the Ba, Nb, and O atoms are extremely weak; this might be due to a lack of unpaired electrons.[63] The quantum confinement effect may be responsible for the negative MM of the O atom.

3.4. Thermoelectric properties

The thermoelectric features of all these compositions were computed using the BoltzTrap code, and Fig. 6(a–d) display a pictorial representation of the thermoelectric parameters in the temperature range of 100–400 K.[64] In the present investigations, we calculated the thermoelectric properties using the BoltzTrap code, with the relaxation time taken as 10^{-14} s and kept constant for the whole electronic gas system. The theory behind the computation of thermoelectric features is classical Boltzmann theory in which relaxation time (τ) is kept constant, *i.e.*, 10^{-14} s. The carrier concentration ~10^{19} was used in the calculations of the thermoelectric parameters. The computed electrical conductivity (σ) of the Ba_2XNbO_6 (X = V, Cr, Mn, and

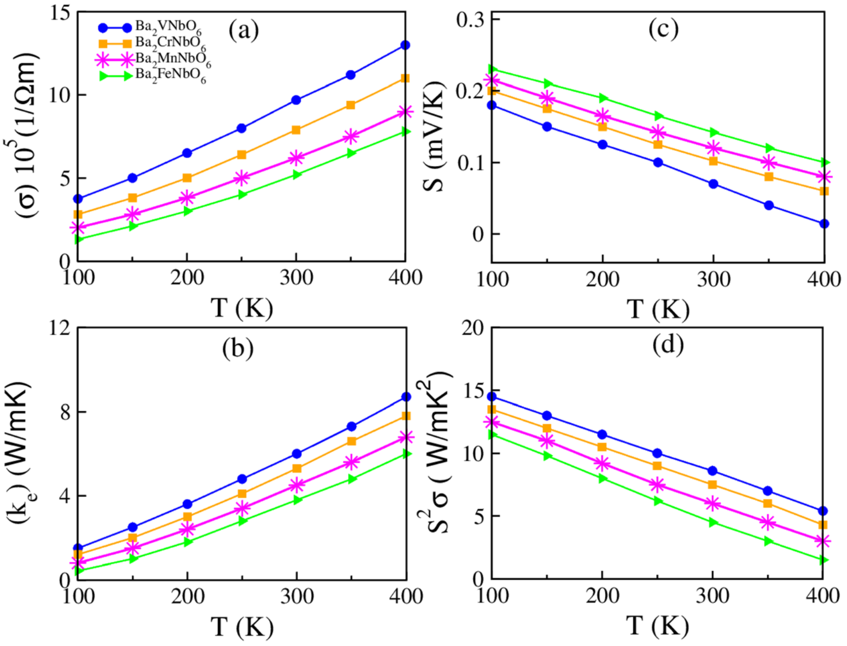

Fig. 6 (a) The electrical conductivity, (b) electronic part of thermal conducctivity, (c) Seebeck coefficient and (d) power factor of Ba_2XNbO_6 (X = V, Cr, Mn, Fe) in the temperature range of 100–400 K.

Fe) double perovskite series exhibits a monotonic, nearly linear increase with rising temperature in the range of 100–400 K, indicating enhanced carrier mobility or thermally activated transport mechanisms. To accurately evaluate the thermoelectric response, it is essential to consider the contributions from both the up- and down-spin configurations. Accordingly, key thermoelectric transport parameters, such as electrical conductivity (σ), electronic contribution to thermal conductivity (κ_e), and the Seebeck coefficient (S), were computed using spin-averaged formulations, given by eqn (4)–(6) as follows:

$$\sigma = \frac{\sigma(\uparrow) + \sigma(\downarrow)}{2}, \tag{4}$$

$$k = \frac{k(\uparrow) + k(\downarrow)}{2}, \tag{5}$$

$$S = \frac{\sigma(\uparrow)S(\uparrow) + \sigma(\downarrow)S(\downarrow)}{\sigma(\uparrow) + \sigma(\downarrow)}. \tag{6}$$

Fig. 6(a) shows the electrical conductivities of the studied compounds calculated against the temperature, and their range is set at 100 to 400 K. It is observed from the graph that the electrical conductivity increased with temperature for all compositions, revealing that these materials show a semiconducting character in this given range of temperature. This might be attributed to the presence of thermally activated charge carriers in all compositions.[65] At room temperature, the values of the electrical conductivities are 9.70×10^5 Ωm^{-1} for Ba_2VNbO_6, 7.90×10^5 Ωm^{-1} for Ba_2CrNbO_6, 6.20×10^5 Ωm^{-1} for Ba_2MnNbO_6, and 5.21×10^5 Ωm^{-1} for Ba_2FeNbO_6. These values indicate that the V-based composition exhibited better electronic conductivity compared to the other compositions. A graph of the thermal conductivity *versus* temperature is depicted in Fig. 6(b). The κ_e also increased when raising the temperature for all compounds, indicating that these materials have more thermally excited free electrons because of raised thermal vibrations.[66] The computed κ_e values are noted as 6.0, 5.30, 4.50, and 3.81 W mK^{-1} for the V, Cr, Mn, and Fe-based compositions, respectively, at room temperature, revealing that the V-based composition shows greater κ_e than the other compositions. Furthermore, the potential gradient between the contacts of the various metals is explained by the Seebeck coefficient (S).[67] The S is measured in mV K^{-1}, as demonstrated in Fig. 6(c). At a temperature of 100 K, the values of S are 0.23 mV K^{-1}, 0.21 mV K^{-1}, 0.2 mV K^{-1}, and 0.18 mV K^{-1} for the Fe, Mn, Cr, and V-based compositions, respectively, which reveals that the Fe-based composition possesses the highest S compared to the rest of the compositions. For all compositions, the S value decreases as temperature increases, indicating that the mobility of the charge carriers decreases due to increased electron-phonon interaction at elevated temperatures.[68] Furthermore, all the studied compositions exhibited a p-type nature, confirmed by the positive values of S. Moreover, the calculated values of S at room temperature are 0.142 mV K^{-1}, 0.120 mV K^{-1}, 0.102 mV K^{-1}, and 0.070 mV K^{-1} for Fe, Mn, Cr, and V, respectively. In addition, the power factor (PF) was computed, as the product of σ and S^2, to check the performance of the studied compounds. Fig. 6(d) displays the observed values of the PF. A decreasing trend is observed from the graph of the PF. The reason behind this decrease in the PF is a decrease in S and the mobility of the charge carriers.[69] The calculated values of PF at room temperature are 8.60 W mK^{-2}, 7.50 W mK^{-2}, 6.00 W mK^{-2}, and 4.51 W mK^{-2} for the V, Cr, Mn, and Fe-based compositions, respectively, suggesting that the V-based composition shows a higher value of PF and thus demonstrates a higher capability of conversion of heat energy to electrical energy.[70]

Lattice vibrations significantly influence thermal management, operational stability, and the overall efficiency of materials employed in spintronic and thermoelectric technologies. To quantitatively evaluate this aspect, the lattice thermal conductivity κ_L of the investigated compositions was computed using the ShengBTE package, which solves the phonon Boltzmann transport equation from first principles. As shown in Fig. 7, the calculated κ_L values remain consistently low over a wide temperature range, including both ambient and elevated conditions. This pronounced suppression of phonon-mediated heat transport suggests strong anharmonic lattice interactions or phonon-scattering mechanisms intrinsic to the crystal structure. The ultralow lattice thermal conductivity underscores the thermal robustness of the materials and positions them as promising candidates for thermoelectric energy conversion and stable spintronic device applications, where efficient heat dissipation and reduced thermal conductivity are critical performance criteria.[28]

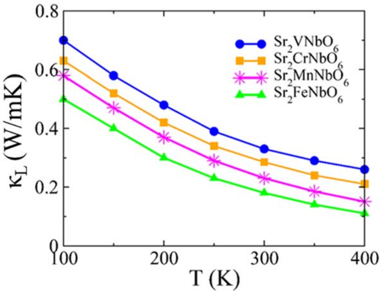

Fig. 7 Lattice thermal conductivity (κ_L) plots of Ba_2XNbO_6 (X = V, Cr, Mn, and Fe).

4. Conclusion

In the current research, we examined the structural, electronic, magnetic, and thermoelectric properties of Ba_2XNbO_6 (X = V, Cr, Mn, and Fe) using DFT. The comparison of the energies of the AFM and FM states confirms the stability of the FM states. The formation enthalpies of the FM states were negative, confirming their thermodynamic stability. Curie temperatures decreased from 325 K for Ba_2VNbO_6 to 289 K for Ba_2FeNbO_6, which shows that magnetic interactions become weaker with more 3d-electrons present. According to their electronic structures, Ba_2VNbO_6 and Ba_2MnNbO_6 were half-metallic ferromagnets, but Ba_2CrNbO_6 and Ba_2FeNbO_6 were classified as ferromagnetic semiconductors. The total magnetic moment increased from $2.00\mu_B$ (V) to $5.00\mu_B$ (Fe) because more electrons were placed in the 3d orbitals. The distribution of MM to non-magnetic sites and complete spin polarizations ensures ferromagnetism by the spin of electrons instead of the accumulation of magnetic ions. The crystal field energy is overcome by the exchange of energies of 3d and 4d electrons. Furthermore, the negative values of the p–d coupling and its exchange constants lower the energy of the system to stabilize the ferromagnetism. Analysis of thermoelectric measurements revealed that Ba_2VNbO_6 has a record power factor (8.60 W mK^{-2}) because of its high electrical conductivity and balanced Seebeck coefficient. Based on these findings, future studies can consider A-site or oxygen-site doping, different types of strain engineering, and heterostructure formation to boost spin polarization, achieve Curie temperatures that are higher than room temperature, and enhance thermoelectric performance, contributing to next-generation energy and spintronic devices. Ba_2VNbO_6 has the highest value of the power factor, which recommends it for thermoelectric applications.

Conflicts of interest

There is no conflict to declare.

Data availability

All data included in this paper will be made available upon request.

Acknowledgements

The authors extend their appreciation to the Deanship of Research and Graduate Studies at King Khalid University for funding this work through a Large Research Project under the grant number RGP2/355/47. The authors extend their appreciation to the Deanship of Scientific Research at Northern Border University, Arar, KSA for funding this research work through the project number “NBU-FFR-2026-674-08”.

References

1 M. H. Cherif, M. Houari, B. Bouadjemi, S. Haid, S. Bentata, T. Lantri, *et al.*, Unveiling Ba_2NiUO_6 as a stable cubic double perovskite with promising spintronic and energy conversion capabilities, *Indian J. Phys.*, 2026, 1–16.

2 W. Kang, Y. Zhang, Z. Wang, J. O. Klein, C. Chappert, D. Ravelosona, *et al.*, Spintronics: emerging ultra-low-power circuits and systems beyond MOS technology, *ACM J. Emerg. Technol. Comput. Syst.*, 2015, **12**(2), 1–42.

3 K. Inomata, N. Ikeda, N. Tezuka, R. Goto, S. Sugimoto, M. Wojcik, *et al.*, Highly spin-polarized materials and devices for spintronics, *Sci. Technol. Adv. Mater.*, 2008, **9**(1), 014101.

4 R. A. De Groot, F. M. Mueller, P. V. van Engen and K. H. J. Buschow, New class of materials: half-metallic ferromagnets, *Phys. Rev. Lett.*, 1983, **50**(25), 2024.

5 J. Xu, C. Xu, J. B. Liu, L. Bellaiche, H. Xiang, B. X. Liu, *et al.*, Prediction of room-temperature half-metallicity in layered halide double perovskites, *npj Comput. Mater.*, 2019, **5**(1), 114.

6 S. Niaz, M. A. Khan, N. A. Noor, A. Mahmood, Y. M. Alanazi and S. Mumtaz, Analysis of structural stability and half metallic ferromagnetism of Cs_2VX_6 (X = Cl, Br) double perovskites for spintronic applications: ab-initio simulations, *ECS J. Solid State Sci. Technol.*, 2023, **12**(9), 093004.

7 S. M. Thompson, The discovery, development and future of GMR: the Nobel Prize 2007, *J. Phys. D Appl. Phys.*, 2008, **41**(9), 093001.

8 Q. Mahmood, Study of influence of electron spin on half metallic ferromagnetism and thermoelectric behavior of X_2TiMoO_6 (X = Mg, Ca, Sr, Ba) for spintronic applications, *J. Inorg. Organomet. Polym. Mater.*, 2026, **36**(2), 1311–1324.

9 W. E. Pickett and D. J. Singh, Electronic structure and half-metallic transport in the $La_{1-x}Ca_xMnO_3$ system, *Phys. Rev. B: Condens. Matter Mater. Phys.*, 1996, **53**, 1146–1151.

10 X. L. Zhang, L. F. Liu and W. M. Liu, Quantum anomalous Hall effect and tunable topological states in 3d transition metals doped silicene, *Sci. Rep.*, 2013, **3**, 2908.

11 H. Liu, S. Y. Wu, R. Singh, L. Gu, D. J. Smith, N. Newman, *et al.*, Observation of ferromagnetism above 900 K in CrGaN and CrAlN, *Appl. Phys. Lett.*, 2004, **85**, 4076–4078.

12 Y. Lu, Q. Wang, L. Han, Y. Zhao, Z. He, W. Song, *et al.*, Spintronic phenomena and applications in hybrid organic–inorganic perovskites, *Adv. Funct. Mater.*, 2024, **34**(27), 2314427.

13 W. L. Warren, K. Vanheusden, D. Dimos, G. E. Pike and B. A. Tuttle, Oxygen vacancy motion in perovskite oxides, *J. Am. Ceram. Soc.*, 1996, **79**(2), 536–538.

14 H. Murtaza, Q. Ain, J. Munir, H. M. Ghaithan, A. A. A. Ahmed, A. S. Aldwayyan, *et al.*, Effect of bandgap tunability on the physical attributes of potassium-based K_2CuBiX_6 (X = I, Br, Cl) double perovskites for green technologies, *Inorg. Chem. Commun.*, 2024, **162**, 112206.

15 S. M. Qaid, Q. ul Ain, H. M. Ghaithan, I. Mursaleen, A. A. A. Ahmed, J. Munir, *et al.*, First-principles investigations on the structural, optoelectronic, mechanical and transport properties of new stable lead-free double perovskites $Cs_2BB'I_6$ (B = Ag/Rb, B′ = Bi/Ga) halides, *Mater. Sci. Eng., B*, 2024, **301**, 117176.

16 C. W. Zhang and S. S. Yan, First-principles study on ferromagnetism in Mg-doped SnO_2, *Appl. Phys. Lett.*, 2009, **95**, 232108.

17 A. Winkler, N. Narayanan, D. Mikhailova, K. G. Bramnik, H. Ehrenberg, H. Fuess, *et al.*, Magnetism in Re-based ferrimagnetic double perovskites, *New J. Phys.*, 2009, **11**, 073047.

18 P. Majewski, S. Geprägs, O. Sanganas, M. Opel, R. Gross, F. Wilhelm, *et al.*, X-ray magnetic circular dichroism study

of Re 5d magnetism in Sr_2CrReO_6, *Appl. Phys. Lett.*, 2005, **87**, 20.

19 Z. Fang, K. Terakura and J. Kanamori, Strong ferromagnetism and weak antiferromagnetism in double perovskites: Sr_2FeMO_6 (M = Mo, W, and Re), *Phys. Rev. B: Condens. Matter Mater. Phys.*, 2001, **63**, 180407.

20 Y. Krockenberger, M. Reehuis, M. Tovar, K. Mogare, M. Jansen and L. Alff, A neutron scattering study of the crystal and magnetic structure of Sr_2CrOsO_6, *J. Magn. Magn. Mater.*, 2007, **310**, 1854–1856.

21 O. Sahnoun, H. Bouhani-Benziane, M. Sahnoun and M. Driz, Magnetic and thermoelectric properties of ordered double perovskite Ba_2FeMoO_6, *J. Alloys Compd.*, 2017, **714**, 704–708.

22 S. A. Khandy and D. C. Gupta, Electronic structure, magnetism and thermoelectric properties of double perovskite Sr_2HoNbO_6, *J. Magn. Magn. Mater.*, 2018, **458**, 176–182.

23 L. F. Blaha, A. Maaf, H. Rozale, A. Chahed, M. A. H. Boukli and A. Sayade, First-principles calculations of structural, magneto-electronic, elastic, mechanical, and thermoelectric properties of half-metallic double perovskite oxide Sr_2TiCoO_6, *Rev. Mex. Fis.*, 2021, **67**(1), 114–122.

24 M. Agouri, A. Waqdim, A. Abbassi, M. Ouali, S. Taj, B. Manaut, *et al.*, Thermoelectric, magneto-electronic, and mechanical properties of new X_2CeVO_6 (X = Sr, Ba) double perovskites for thermoelectric and spintronic applications, *Eur. Phys. J. B*, 2024, **97**(3), 27.

25 Q. Mahmood, Study of half metallic ferromagnetism, Curie temperature, and thermoelectric aspects of double perovskite oxides Ba_2XMoO_6 (X = Cr, Mn, Fe, Co) for spintronic applications, *Mater. Sci. Semicond. Process.*, 2025, **193**, 109519.

26 M. Caid, Y. Rached, D. Rached and H. Rached, First-principles study of the structural, elastic, magneto-electronic and thermoelectric properties of double perovskite Ba_2ZrFeO_6 in ferrimagnetic phase, *Comput. Condens. Matter*, 2023, **37**, e00847.

27 M. Ishfaq, A. R. Iftikhar, H. Ali, K. Ismail, G. Murtaza, G. A. Al-Hazmi, *et al.*, Theoretical analysis of double perovskite A_2HfNiO_6 (A = Ba, Ca, Sr) for structural, elastic, optical, electronic, thermoelectric and magnetic properties for spintronics applications, *Mater. Sci. Eng., B*, 2025, **317**, 118198.

28 S. A. Khandy and D. C. Gupta, Insight view of double perovskites Ba_2XNbO_6 (X = Ho, Yb) for spintronics and thermoelectric applications, *Int. J. Energy Res.*, 2021, **45**(9), 13338–13354.

29 M. H. Cherif, L. Beldi, M. Houari, B. Bouadjemi, S. Bentata, S. Haid, *et al.*, Investigating the multifaceted characteristics of Ba_2FeWO_6 double perovskite: insights from density functional theory, *J. Mol. Graph. Model.*, 2024, **132**, 108834.

30 R. Ullah, M. A. Ali, B. U. Haq, A. Khan, Q. Mahmood and G. Murtaza, Exploring electronic, structural, magnetic, and thermoelectric properties of novel Ba_2EuMoO_6 double perovskite, *Mater. Sci. Semicond. Process.*, 2022, **137**, 106218.

31 A. Ali, Q. Rafiq, G. Khan, S. S. Hayat, S. Azam, M. Aamer, *et al.*, Exploring the magneto-optic, thermoelectric, and electronic properties of Ba_2GdXO_6 (X = Nb, U) double perovskites by employing the DFT approach, *Chem. Pap.*, 2025, **79**(2), 1137–1153.

32 S. Nadeem, Q. Mahmood, M. Hassan, N. D. Alkhaldi, A. Akremi, H. E. Ali, *et al.*, Study of half metallic ferromagnetism and transport properties of Sr_2NbXO_6 (X = Mn, Fe, Co, Ni) for spintronics and energy harvesting applications, *Mater. Chem. Phys.*, 2025, 131051.

33 M. Sun, Q. Ren, Y. Zhao, J. P. Chou, J. Yu and W. Tang, Electronic and magnetic properties of 4d series transition metal substituted graphene: a first-principles study, *Carbon*, 2017, **120**, 265–273.

34 M. Sun, Q. Ren, Y. Zhao, S. Wang, J. Yu and W. Tang, Magnetism in transition metal-substituted germanane: a search for room temperature spintronic devices, *J. Appl. Phys.*, 2016, **119**, 143904.

35 J. Yang, Y. Zhou, Y. Dedkov and E. Voloshina, Dirac fermions in half-metallic ferromagnetic mixed $Cr_{1-x}M_xPSe_3$ monolayers, *Adv. Theory Simul.*, 2020, **3**(12), 2000228.

36 Z. Zhang, X. Lin, J. Lin, N. Liu, B. Wan, X. Fang, *et al.*, Cellulose supported and strengthened shear stiffening gel with enhanced impact-resistant performance, *Chem. Eng. J.*, 2023, **473**, 145435.

37 P. Blaha, K. Schwarz, G. K. Madsen, D. Kvasnicka and J. Luitz, *WIEN2k: an augmented plane wave + local orbitals program for calculating crystal properties*, 2001, vol. 60, no. 1, pp. 155–169.

38 J. P. Perdew, K. Burke and M. Ernzerhof, Generalized gradient approximation made simple, *Phys. Rev. Lett.*, 1997, **78**, 139.

39 G. I. Csonka, J. P. Perdew, A. Ruzsinszky, P. H. Philipsen, S. Lebègue, J. Paier, *et al.*, Assessing the performance of recent density functionals for bulk solids, *Phys. Rev. B: Condens. Matter Mater. Phys.*, 2009, **79**, 155107.

40 F. Tran and P. Blaha, Accurate band gaps of semiconductors and insulators with a semi-local exchange-correlation potential, *Phys. Rev. Lett.*, 2009, **102**, 226401.

41 H. Zaari, A. G. El Hachimi, A. Benyoussef and A. El Kenz, Comparative study between TB-mBJ and GGA+U on magnetic and optical properties of $CdFe_2O_4$, *J. Magn. Magn. Mater.*, 2015, **393**, 183–187.

42 W. Li, C. F. J. Walther, A. Kuc and T. Heine, Density functional theory and beyond for band-gap screening: performance for transition-metal oxides and dichalcogenides, *J. Chem. Theory Comput.*, 2013, **9**, 2950–2958.

43 G. K. Madsen and D. J. Singh, BoltzTraP: a code for calculating band-structure dependent quantities, *Comput. Phys. Commun.*, 2006, **175**, 67–71.

44 K. Esfarjani and J. Shiomi, Fundamentals and advances in thermal transport in thermoelectric materials, *MRS Bull.*, 2025, **50**(8), 935–944.

45 N. A. Noor, M. Rashid, S. M. Alay-e-Abbas, M. Raza, A. Mahmood, S. M. Ramay, *et al.*, Shift of indirect–direct band gap and the thermoelectric response of cubic $BiScO_3$

via DFT-mBJ studies, *Mater. Sci. Semicond. Process.*, 2016, **49**, 40–47.

46 M. Wu, Y. Han, A. Bouhemadou, Z. Cheng, R. Khenata, M. Kuang, *et al.*, Site preference and tetragonal distortion in palladium-rich Heusler alloys, *IUCrJ*, 2019, **6**(2), 218–225.

47 N. Sharma, D. Chandra, A. Rathi and A. K. Singh, First-principles WC-GGA and mBJ calculations for structural, electronic, optical, and elastic properties of $M_xGa_{1-x}Sb$ (M = Al, In, B) ternary alloys, *Mater. Sci. Semicond. Process.*, 2022, **151**, 107033.

48 F. Birch, Finite elastic strain of cubic crystals, *Phys. Rev.*, 1947, **71**, 809–824.

49 A. Winkler, N. Narayanan, D. Mikhailova, K. G. Bramnik, H. Ehrenberg, H. Fuess, *et al.*, Magnetism in Re-based ferrimagnetic double perovskites, *New J. Phys.*, 2009, **11**, 073047.

50 P. K. Lam, M. L. Cohen and G. Martinez, Analytic relation between bulk moduli and lattice constants, *Phys. Rev. B: Condens. Matter Mater. Phys.*, 1987, **35**, 9190–9193.

51 L. Hnamte and R. K. Thapa, Study of electronic and optical properties of vanadium-based double perovskite oxide: Ba_2VNbO_6, *Int. J. Comput. Eng. Res.*, 2018, **8**(6), 67–71.

52 N. Rama, J. B. Philipp, M. Opel, K. Chandrasekaran, V. Sankaranarayanan, R. Gross, *et al.*, Study of magnetic properties of $A_2B'NbO_6$ (A = Ba, Sr, BaSr; B′ = Fe and Mn) double perovskites, *J. Appl. Phys.*, 2004, **95**(11), 7528–7530.

53 M. Arshad, S. A. Aldaghfag, S. Saleem and M. Yaseen, Electronic, optical and thermoelectric properties of Cs_2XInCl_6 (X = Ag, Na) halide double perovskites, *Phys. Status Solidi B*, 2024, **261**(2), 2300265.

54 V. Y. Irkhin and M. I. Katsnelson, Half-metallic ferromagnets, *Phys. Usp.*, 1994, **37**(7), 659–676.

55 T. Dietl, Ferromagnetic semiconductors, *Semicond. Sci. Technol.*, 2002, **17**(4), 377–392.

56 J. H. Van Vleck, On the magnetic behavior of vanadium, titanium and chrome alum, *J. Chem. Phys.*, 1939, **7**(1), 61–71.

57 M. Wang, C. Li, X. G. Li and Y. Hou, Direct observation of strong t_{2g}–e_g orbital hybridization and effects of f orbitals in a molecular analogue of chromium perovskite, *Phys. Rev. B*, 2024, **110**(2), L020409.

58 C. J. Sansonetti, J. Reader, A. Tauheed and Y. N. Joshi, Spectrum and energy levels of triply ionized barium (Ba IV), *J. Opt. Soc. Am. B*, 1993, **10**(1), 7–12.

59 M. Lenglet, Iono-covalent character of the metal-oxygen bonds in oxides: a comparison of experimental and theoretical data, *Act. Passive Electron. Compon.*, 2004, **27**(1), 1–60.

60 G. M. Mustafa, B. A. El-Badry, S. Rafique, N. D. Alkhaldi, Q. Mahmood, S. Bouzgarrou, *et al.*, Investigation of above room temperature ferromagnetism and thermoelectric characteristics of double perovskites $Sr_2(Fe/Co)MoO_6$ for spintronic applications, *Phys. B*, 2026, 418737.

61 Q. Mahmood, T. Alshahrani, B. U. Haq, Q. Gulfam, Y. Tahir, N. A. Kattan, *et al.*, Role of 5d orbital of Re in ferromagnetism and thermoelectric characteristics of Cs_2ReCl/Br_6 double perovskites: a density functional theory study, *Eur. Phys. J. Plus*, 2020, **135**, 727.

62 S. K. Singh, J. Eng, M. Atanasov and F. Neese, Covalency and chemical bonding in transition metal complexes: an ab initio based ligand field perspective, *Coord. Chem. Rev.*, 2017, **344**, 2–25.

63 Q. Mahmood, S. A. Ali, M. Hassan and A. Laref, First-principles study of ferromagnetism, optical and thermoelectric behaviors of AVO_3 (A = Ca, Sr, Ba) perovskites, *Mater. Chem. Phys.*, 2018, **211**, 428–437.

64 T. Takagahara and K. Takeda, Theory of the quantum confinement effect on excitons in quantum dots of indirect-gap materials, *Phys. Rev. B: Condens. Matter Mater. Phys.*, 1992, **46**, 15578–15584.

65 A. Bupu, M. A. Majidi and A. Rusydi, Theoretical study on the magnetic moment's formation in Ta-doped anatase TiO_2, *Mater. Sci. Eng., B*, 2017, **188**, 012009.

66 S. A. Dar, V. Srivastava and U. K. Sakalle, Structural, elastic, mechanical, electronic, magnetic, thermoelectric and thermodynamic investigation of half metallic double perovskite oxide Sr_2MnTaO_6, *J. Magn. Magn. Mater.*, 2019, **484**, 298–306.

67 S. A. Dar, V. Srivastava, U. K. Sakalle and G. Pagare, Insight into electronic structure, magnetic, mechanical and thermodynamic properties of double perovskite Ba_2MgReO_6: a first-principles investigation, *Comput. Condens. Matter*, 2018, **14**, 137–143.

68 H. W. Eng, P. W. Barnes, B. M. Auer and P. M. Woodward, Investigations of the electronic structure of d0 transition metal oxides belonging to the perovskite family, *J. Solid State Chem.*, 2003, **175**(1), 94–109.

69 W. Gouasmia, D. Boudjaadar, F. Oumelaz, O. Nemiri, A. Boumaza, R. Benredouane, *et al.*, DFT study of Ca_2NaXO_6 (X = Cl or Br) double perovskites: structural, electronic, mechanical, thermoelectric, and optical properties, *Phys. Solid State*, 2026, **68**(4), 320–336.

70 T. J. Slade, J. A. Grovogui, J. J. Kuo, S. Anand, T. P. Bailey, M. Wood, *et al.*, Understanding the thermally activated charge transport in $NaPb_mSbQ_{m+2}$ (Q = S, Se, Te) thermoelectrics: weak dielectric screening leads to grain boundary dominated charge carrier scattering, *Energy Environ. Sci.*, 2020, **13**(5), 1509–1518.